PERGAMON

International Journal of Multiphase Flow 27 (2001) 277–298

International Journal of Multiphase Flow

www.elsevier.com/locate/ijmulflow

Direct calculation of bubble growth, departure, and rise in nucleate pool boiling

Han Young Yoon*, Seiichi Koshizuka, Yoshiaki Oka

Nuclear Engineering Research Laboratory, Graduate School of Engineering, The University of Tokyo, 2-22 Shirane, Shirakata, Tokai-mura, Naka-gun, Ibaraki 319-1106, Japan

Received 7 September 1999; received in revised form 13 March 2000

Abstract

A mesh-free numerical method (MPS–MAFL) is presented for the analysis of gas–liquid two-phase flows. In this method, a particle method (MPS) is combined with a gridless method (MAFL) for an arbitrary-Lagrangian–Eulerian calculation. Gas–liquid two-phase flows are calculated directly by the present method with and without the phase change. As an isothermal flow, a gas bubble rising in viscous liquids is simulated numerically and the results are compared with the empirical correlation. The energy equation is coupled with the equation of motion for the calculation of nucleate pool boiling. Numerical results are provided for the bubble growth rate, departure radius, and the heat transfer rate, which show a good agreement with experimental observations. The heat transfer mechanism associated with nucleate pool boiling is evaluated quantitatively and discussed with previous empirical studies.

Keywords: Particle–gridless method; Moving interface; Nucleate pool boiling

1. Introduction

Two-phase flows with boiling are fundamental and important phenomena in many engineering problems as chemical or power plants. For example, in the field of nuclear engineering, a good knowledge on the thermal-hydraulics of two-phase flows is a basis for the design and the safety analysis of a light water reactor. However, the mechanisms of mass,

* Corresponding author.

0301-9322/01/$ - see front matter
PII: S0301-9322(00)00023-9

momentum, and energy transfers through the two-phase interface are extremely complicated and their numerical models largely depend upon relevant empirical correlations for a wide range of operating and design conditions. In the present study, a correlation-free numerical method is proposed for the direct calculation of a bubble growth in nucleate pool boiling.

Several analytical and numerical studies on nucleate boiling were presented. For a homogeneous temperature field, Plesset and Zwick (1954) presented a one-dimensional analytical solution of the equation of motion for a spherical bubble (Rayleigh, 1917). Lee and Nydahl (1989) conducted a numerical study of bubble growth in nucleate boiling, where the heterogeneous temperature field and the hydrodynamics were solved assuming a hemispherical shape for the vapor bubble. The direct calculation of the moving phase interface in nucleate pool boiling was realized by Welch (1995), where the finite volume method was applied on a moving unstructured mesh. However, the calculation was limited to a small deformation of the phase interface due to the numerical instability caused by a severe distortion of the computational grid.

It is essential, for a direct calculation of the two-phase flow without empirical correlations, to trace two-phase interfaces accurately, since a physical quantity is discontinuous at the interface. In the finite difference methods such as marker-and-cell (Welch et al., 1966) and volume-of-fluid (Hirt and Nichols, 1981) methods, the moving interface is traced with marker particles or functions that are advected through the finite difference mesh. In these methods, the physical quantity at a computing cell implying a phase interface is calculated by volumetric averaging of vapor and liquid phases. Thus the discontinuous phase interface is likely to be smoothed out. Besides the problem concerning the moving interface, the steep temperature profile near the moving phase interface should be calculated for the analysis of nucleate boiling. A fine computational mesh has to be generated adaptively along the moving boundary for the calculation of this thermal layer. This is difficult in the conventional finite difference methods since they are usually implemented on rectangular Eulerian grids. The numerical schemes such as arbitrary-Lagrangian–Eulerian (ALE) by Hirt et al. (1974), the boundary-fitted-coordinates (BFC) by Ryskin and Leal (1983), and the finite volume method (FVM) by Rhie and Chow (1983) have an advantage since their mesh can be generated to fit the interface shape. The discontinuity of the phase interface could be accurately resolved in these methods. The generation of interface-fitted mesh, however, is troublesome when the interface deforms largely.

In this paper, we present a mesh-free numerical method for direct calculation of bubble growth. It is a combination of particle and gridless methods where the terms, 'particle' and 'gridless', refer to Lagrangian and Eulerian schemes, respectively. Thus, an arbitrary-Lagrangian–Eulerian calculation is possible, in this method, with a cloud of computing points that are equivalent to the computing cells in mesh-based methods. The moving interface is traced through the Lagrangian motion of the computing points using a particle method and, at the fixed computing points, convection is calculated using a gridless method. The particle interaction model of the moving-particle semi-implicit (MPS) method (Koshizuka and Oka, 1996) is applied to the differential operators and the meshless-advection using flow-directional local-grid (MAFL) scheme (Yoon et al., 1999) is utilized for the gridless method. A complex moving interface problem can be effectively analyzed by MPS–MAFL since the mesh is no longer used. Using the present method, numerical analyses are provided for a single bubble in

both isothermal and nucleate pool boiling conditions. The heat transfer mechanism of nucleate pool boiling is discussed quantitatively based on the numerical results. All the calculations are carried out in x–y two-dimensional coordinates except for the heat transfer estimation where the liquid volume is computed assuming an axisymmetric condition.

2. Governing equations

The continuity, Navier–Stokes and energy equations for incompressible viscous flows are

$$\nabla \cdot \mathbf{u} = 0, \tag{1}$$

$$\rho\left(\frac{\partial \mathbf{u}}{\partial t} + (\boldsymbol{u} - \mathbf{u}^{c}) \cdot \nabla \mathbf{u}\right) = -\nabla p + \mu \nabla^2 \mathbf{u} + \sigma\kappa \cdot \mathbf{n} + \rho \mathbf{g}, \tag{2}$$

and

$$\frac{\partial T}{\partial t} + (\mathbf{u} - \mathbf{u}^{c}) \cdot \nabla T = \alpha \nabla^{2} T \tag{3}$$

where ρ is liquid density, μ is viscosity, σ is surface tension constant, κ is curvature of the interface, $\mathbf{n}$ is unit normal vector to the interface, T is temperature, and α is thermal diffusivity. In the convection terms of Eqs. (2) and (3), $\mathbf{u}$ is the fluid velocity and $\mathbf{u}^{c}$ represents the motion of a computing point that is adaptively configured during the calculation. An arbitrary calculation is allowed between fully Lagrangian ($\mathbf{u}^{c} = \mathbf{u}$) and Eulerian ($\mathbf{u}^{c} = 0$) calculations so that a sharp fluid front is calculated accurately by moving the computing point in Lagrangian coordinates while the fixed boundaries are described with Eulerian coordinates.

3. The numerical method

The calculation procedure consists of three phases — Lagrangian, re-configuration, and convection (Eulerian) phases. In the first phase, the right side of Eq. (2) is solved explicitly and the temporal velocity, $\mathbf{u}^{*}$, is obtained by

$$\mathbf{u}^{*} = \mathbf{u}^{n} + \frac{\Delta t}{\rho}\left[\mu \nabla^2 \mathbf{u}^{n} + \sigma(\kappa \cdot \mathbf{n})^{n} + \rho \mathbf{g}\right] \tag{4}$$

where the superscript 'n' refers to time level and Δt is time increment. Then the temporal location of the computing point becomes

$$\mathbf{r}^{*} = \mathbf{r}^{n} + \mathbf{u}^{*} \Delta t \tag{5}$$

The pressure is calculated implicitly using the continuity equation as in the case of conventional mesh-based methods such as MAC or SIMPLE.

$$\nabla^2 P^{n+1} = \frac{\rho}{\Delta t}\nabla \cdot \mathbf{u}^* \tag{6}$$

The temporal velocity is updated by the pressure gradient as

$$\frac{\mathbf{u}^{\mathrm{L}} - \mathbf{u}^*}{\Delta t} = -\frac{1}{\rho}\nabla P^{n+1} \tag{7}$$

and the position of the computing point is replaced by

$$\mathbf{r}^{\mathrm{L}} = \mathbf{r}^n + \mathbf{u}^{\mathrm{L}}\Delta t \tag{8}$$

where the superscript 'L' stands for the Lagrangian description. The temperature at $\mathbf{r}^{\mathrm{L}}$ is obtained by solving Eq. (3) explicitly as

$$T^{\mathrm{L}} = T^n + \alpha\nabla^2 T^n \cdot \Delta t. \tag{9}$$

The particle interaction models of the MPS method, which will be presented in Section 3.1, are applied to the calculation of the differential operators, ∇ and ∇^2, in Eqs. (4), (6), (7) and (9). Large topological changes in fluids such as dam collapse (Koshizuka and Oka, 1996), fluid-structure interaction (Koshizuka and Oka, 1998) and the fragmentation process in steam explosion (Ikeda et al., 1996) were successfully analyzed using MPS.

In the re-configuration phase, the new-time positions, $\mathbf{r}^{n+1}$, are determined by adjusting the configuration of computing points at $\mathbf{r}^{\mathrm{L}}$ and the velocity of a computing point, $\mathbf{u}^c$, is calculated by

$$\mathbf{u}^c = \frac{\mathbf{r}^{n+1} - \mathbf{r}^n}{\Delta t}. \tag{10}$$

From Eqs. (8) and (10), the arbitrary convection velocity $\mathbf{u}^{\mathrm{a}}$ becomes

$$\frac{\mathbf{r}^{\mathrm{L}} - \mathbf{r}^n}{\Delta t} - \frac{\mathbf{r}^{n+1} - \mathbf{r}^n}{\Delta t} = -\frac{\mathbf{r}^{n+1} - \mathbf{r}^{\mathrm{L}}}{\Delta t}. \tag{11}$$

The position changes associated with the velocities $\mathbf{u}^{\mathrm{L}}$, $\mathbf{u}^c$ and $\mathbf{u}^{\mathrm{a}}$ are illustrated in Fig. 1. The re-configuration scheme is discussed in detail in Section 3.2.

Finally, the convection terms of Eqs. (2) and (3) are solved to obtain the values of velocity and temperature at the computing points configured in the second phase. This corresponds to the interpolation of values at $\mathbf{r}^L - \Delta t\mathbf{u}^{\mathrm{a}}$ from the profiles of $\mathbf{u}^{\mathrm{L}}$ and T^{L} as

$$\mathbf{u}^{n+1} \equiv \mathbf{u}(\mathbf{r}^{n+1}) = \mathbf{u}(\mathbf{r}^{\mathrm{L}} - \Delta t\, \mathbf{u}^{\mathrm{a}}) \tag{12}$$

and

$$T^{n+1} \equiv T(\mathbf{r}^{n+1}) = T(\mathbf{r}^{\mathrm{L}} - \Delta t\, \mathbf{u}^{\mathrm{a}}). \tag{13}$$

The gridless convection scheme MAFL is used for the calculation of Eqs. (12) and (13). The description of MAFL will be given in Section 3.3.

The accuracy of MPS–MAFL was tested through the calculation of natural convection in a

square cavity (Koshizuka et al., 2000). In this study, the numerical diffusion was small and the numerical results of MPS–MAFL were on the same level of precision with the conventional finite difference or finite element methods.

3.1. Lagrangian phase

Each differential operator appeared in the governing equation is replaced by the particle interaction model. A particle interacts with its neighboring particles with a weight function $w(r, r_e)$, where r is the distance between two particles and r_e is the radius of interaction area. Here the particle is identical with the computing point in Eulerian context and the following function is employed for the weight function throughout the study.

$$w(r, r_e) = \begin{cases} \dfrac{r_e}{r} - 1 & (0 \le r < r_e) \\ 0 & (r_e \le r) \end{cases} \tag{14}$$

Since the influential area of the weight function is bounded by r_e, a particle interacts with a finite number of neighboring particles in $r \le r_e$. The radius of interaction area varies in space and time, i.e. $r_e = r_e(\mathbf{r}, t)$ so that the number of particles within r_e is always kept constant. Then the normalization factor at $\mathbf{r}_i$ is defined by

$$n_i = \sum_{j \neq i} w\left(|\mathbf{r}_j - \mathbf{r}_i|, r_{e,\,ij}\right) \tag{15}$$

where $r_{e,ij} = (r_{e,i} + r_{e,j})/2$ is used instead of $r_{e,i}$ for the conservation of physical properties.

The differential operator vector ∇ in the pressure gradient term of Eq. (2) is expressed in terms of scalar quantities of each particle with the weight function of Eq. (14). A gradient vector between two particles i and j possessing scalar quantities ϕ_i and ϕ_j at $\mathbf{r}_i$ and $\mathbf{r}_j$ is simply defined by $(\phi_j - \phi_i)(\mathbf{r}_j - \mathbf{r}_i)/|\mathbf{r}_j - \mathbf{r}_i|^2$. Then the gradient vector at the particle i is given as the

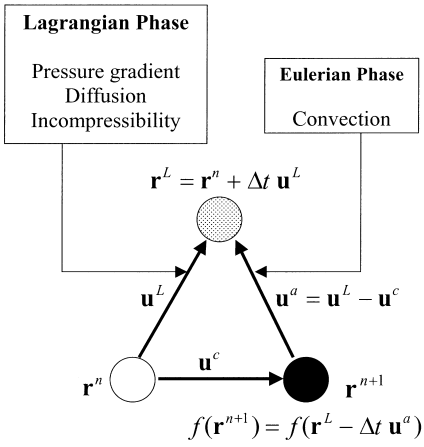

Fig. 1. Schematic diagram of numerical algorithm.

weighted average of the gradient vectors between the particle i and its neighboring particles j,

$$\langle \nabla \phi \rangle_i = \frac{d}{n_i} \sum_{j \neq i} \left[\frac{\phi_j - \phi_i}{|\mathbf{r}_j - \mathbf{r}_i|^2} (\mathbf{r}_j - \mathbf{r}_i) w\big(|\mathbf{r}_j - \mathbf{r}_i|, r_{e,\,ij}\big) \right] \tag{16}$$

where d is the number of space dimensions.

The Laplacian operator ∇^2 representing diffusion is modeled by distribution of a quantity from a particle to its neighboring particles by use of the weight function,

$$\langle \nabla^2 \phi \rangle_i = \frac{2d}{\lambda_i} \sum_{j \neq i} \left[\big(\phi_j - \phi_i\big) w\big(|\mathbf{r}_j - \mathbf{r}_i|, r_{e,\,ij}\big) \right] \tag{17}$$

where

$$\lambda_i = \sum_{j \neq i} \left[|\mathbf{r}_j - \mathbf{r}_i|^2 w\big(|\mathbf{r}_j - \mathbf{r}_i|, r_{e,\,ij}\big) \right]. \tag{18}$$

This Laplacian model is conservative since the quantity lost by the particle i is just obtained by the particle j.

The divergence operator is modeled just like the same way in the gradient model since it is a scalar product of gradient vectors. The velocity divergence between two particles i and j is defined by $(\mathbf{u}_j - \mathbf{u}_i) \cdot (\mathbf{r}_j - \mathbf{r}_i)/|\mathbf{r}_j - \mathbf{r}_i|^2$ and the velocity divergence at the particle i is given by the weighted average of the individual velocity divergences.

$$\langle \nabla \cdot \mathbf{u} \rangle_i = \frac{d}{n_i} \sum_{j \neq i} \left[\frac{(\mathbf{u}_j - \mathbf{u}_i) \cdot (\mathbf{r}_j - \mathbf{r}_i)}{|\mathbf{r}_j - \mathbf{r}_i|^2} w\big(|\mathbf{r}_j - \mathbf{r}_i|, r_{e,\,ij}\big) \right] \tag{19}$$

The right side of Eq. (6) is calculated using Eq. (19) and the left side of Eq. (6) is calculated using the Laplacian model shown in Eq. (17). Then we have simultaneous equations expressed by a linear symmetric matrix. These are solved by the incomplete Cholesky conjugate gradient (ICCG) method. Since this incompressibility model is based on the velocity divergence, the particle number density need not be constant and particles are allowed to be concentrated locally for higher resolution.

Number of space dimension, d, in the gradient and divergence models of Eqs. (16) and (19) is employed to compensate the loss of vertical component of each gradient vectors when they are normalized by n_i. For instance, in a two-dimensional rectangular grid, each component of the gradient vector at point i becomes $\Delta\phi/2$ by Eq. (16) without d. As long as the particle number density is kept constant, the compensation by d does not cause any significant error regardless of the configuration of particles. However, in the present application, the particle distribution is not uniform and the compensation by d in Eqs. (16) and (19) may result in significant error. So the gradient and divergence models should be modified such that normalization factors are computed in x, y, z directions separately instead of using the number of space dimension, d. Then Eqs. (16) and (19) are replaced with

$$\langle \nabla \phi \rangle_{i,\,x} = \frac{1}{n_{i,\,x}} \sum_{j \neq i} \left[\frac{\phi_j - \phi_i}{|\mathbf{r}_j - \mathbf{r}_i|^2} (r_{j,\,x} - r_{i,\,x}) w\big(|\mathbf{r}_j - \mathbf{r}_i|, r_{e,\,ij}\big) \right] \tag{16a}$$

and

$$\langle \nabla \cdot \mathbf{u} \rangle_i = \sum_{j \neq i} \sum_{k=x,\,y,\,z} \frac{(u_{j,\,k} - u_{i,\,k}) \cdot (r_{j,\,k} - r_{i,\,k})}{n_{i,\,k}} \frac{w\big(|\mathbf{r}_j - \mathbf{r}_i|, r_{e,\,ij}\big)}{|\mathbf{r}_j - \mathbf{r}_i|^2} \tag{19a}$$

where

$$n_{i,\,x} = \sum_{j \neq i} \frac{(r_{j,\,x} - r_{i,\,x})^2}{|\mathbf{r}_j - \mathbf{r}_i|^2} w\big(|\mathbf{r}_j - \mathbf{r}_i|, r_{e,\,ij}\big).$$

The second subscripts used in Eqs. (16a) and (19a) represent the x, y, and z components of each vectors of $\mathbf{r}$, $\mathbf{u}$ and $\nabla\phi$, respectively.

Surface tension is implemented by computing the curvature of the phase interface and the pressure gradient, $\nabla p = \sigma\kappa$, is added to the governing equation explicitly. The moving interface is always clearly defined, in the present method, through the Lagrangian motion of the particles on the phase interface and the curvature of the interface can be easily calculated from the configuration of the interface particles.

3.2. Re-configuration phase

The fully Lagrangian method is not adequate for describing inlet or outlet flow boundaries. Also, in the particle method, the fluid front is not clear due to the irregular distribution of the surface particle. Thus, the computing point, particle in Lagrangian context, is re-configured. The physical quantities at new-time position are then interpolated using a convection scheme.

After the positions have been moved from $\mathbf{r}^n$ to $\mathbf{r}^{\mathrm{L}}$ in Lagrangian phase, the computing point belonging to inlet or outlet flow boundaries goes back to its original position, $\mathbf{r}^n$, for a fully Eulerian calculation. In this case, $\mathbf{u}^c$ equals to zero in Eqs. (2) and (3) and the arbitrary convection velocity $\mathbf{u}^{\mathrm{a}}$ coincides with the fluid velocity. On the other hand, the free surface is traced by moving the computing points in Lagrangian description without calculating the convection term. In this case, the position at new-time step, $\mathbf{r}_{\mathrm{surf}}^{n+1}$, simply becomes $\mathbf{r}_{\mathrm{surf}}^{\mathrm{L}}$ where the subscript 'surf' refers to the free surface. However, in practice, $\mathbf{r}_{\mathrm{surf}}^{n+1}$ is slightly moved from $\mathbf{r}_{\mathrm{surf}}^{\mathrm{L}}$ since the computing points are likely to cluster locally in the fully Lagrangian calculation. After the positions of boundary points have been determined, the remaining computing points are configured considering the geometry of boundaries.

The way of configuring the computing point depends on the specific problem. This corresponds to the mesh generation scheme in the conventional mesh-based method. Although it is somewhat laborious task to configure the computing points for a complex geometry, especially in three dimensions, it is much easier in our method and takes less time than generating the mesh structure in the mesh-based method. The number of computing points needs not be kept constant so that one can drop more computing points to improve the local resolution.

Once the positions at new-time step $(n+1)$ are determined, the convection velocity, $\mathbf{u}_i^{\mathrm{a}}$, is calculated by Eq. (11) and the physical properties such as flow velocity and temperature at $\mathbf{r}_i^{n+1}$ are interpolated by a convective calculation of

$$f_i^{n+1} \equiv f\left(\mathbf{r}_i^{n+1}\right) = f\left(\mathbf{r}_i^{\mathrm{L}} - \Delta t \mathbf{u}_i^{\mathrm{a}}\right) \tag{20}$$

where f is $\mathbf{u}$ or T. The number of computing points dose not change in Eq. (20) when they are re-configured since f^{n+1} and f^{L} are defined at the same computing point i. When the number of computing points changes in re-configuration phase, the physical quantities at r_i^{n+1} are determined by

$$f^{n+1}\left(\mathbf{r}_i^{n+1}\right) = f^{\mathrm{L}}\left(\mathbf{r}_o^{\mathrm{L}} - \Delta t \mathbf{u}_i^{\mathrm{a}}\right) \tag{21}$$

where $\mathbf{r}_o^{\mathrm{L}}$ is the closest point to $\mathbf{r}_i^{n+1}$ among all $\mathbf{r}^{\mathrm{L}}$ and $\mathbf{u}_i^{\mathrm{a}} = -(\mathbf{r}_i^{n+1} - \mathbf{r}_o^{\mathrm{L}})/\Delta t$. A computing point at $\mathbf{r}_i^{\mathrm{L}}$ can have a single or multiple upstream points, $\mathbf{r}_i^{\mathrm{n}+1}$, depending on the re-configuration scheme. It is also probable that there exists no upstream point at all.

3.3. Convection phase

Any multi-dimensional convection problem can be regarded as a one-dimensional problem if a computational grid is generated along the flow direction. Considering the flow direction at each computing point ($\mathbf{u}^{\mathrm{a}}$ in Eqs. (12) and (13)), a one-dimensional local grid is generated as shown in Fig. 2 where Δr shows the distance between local grid points and $r_{e,\,i}$ is the radius of interpolation area. The positions of local grid points are denoted by $\langle \mathbf{r} \rangle_k$. Locations and the number of local grid points are determined based on the difference scheme that will be applied to. For example, in Fig. 2, three local grid points are placed (two are in the upstream and the other is in the downstream of a computing point) for the application of a second-order upwind scheme.

For the local grid points on the one-dimensional local grid, the physical properties, $\langle f \rangle_k$, are interpolated from those of neighboring computing points, f_j^{L}, using a weight function as follows.

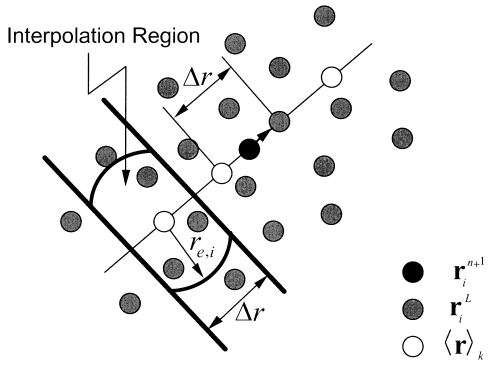

Fig. 2. Generation of local grid.

$$\langle f\rangle_k = \frac{\sum_j f_j^{\mathrm{L}} w\left(|\mathbf{r}_j^{\mathrm{L}} - \langle \mathbf{r}\rangle_k|, r_{e,k}\right)}{\sum_j w\left(|\mathbf{r}_j^{\mathrm{L}} - \langle \mathbf{r}\rangle_k|, r_{e,k}\right)}, \quad k = -2, -1, 1 \tag{22}$$

The weight function in Eq. (14) is utilized for the calculation of Eq. (22). The interpolation region is limited by a circle (sphere for three dimensions) of the radius of interpolation area, $r_{e,k}$, and the grid lines vertical to the flow direction as shown in Fig. 2. If all the particles within the radius of $r_{e,k}$ are used for the interpolation, the interpolation regions would overlap each other and this would cause more numerical diffusion since the more computing points are engaged in Eq. (22) as the interpolation area becomes large.

Any difference scheme can be applied easily since a one-dimensional grid has been obtained along the flow direction. In the present study, a first-order upwind scheme is applied as

$$f_i^{n+1} = f_i^{\mathrm{L}} - q\left(f_i^{\mathrm{L}} - \langle f\rangle_{-1}\right) \tag{23}$$

where $q = |\mathbf{u}^{\mathrm{a}}|\Delta t/\Delta r$, while the QUICK scheme was applied in the previous paper (Yoon et al., 1999). This is because that a higher-order scheme such as QUICK often causes numerical instability when the number and location of the computing point largely change during the re-configuration phase and thus the profile of the convection velocity, $\mathbf{u}^{\mathrm{a}}$, is distorted severely.

4. A rising bubble in viscous liquids

Prior to the boiling problem, the present method is applied first to the isothermal flow of a single bubble rising in viscous fluids. The phase change and heat transfer are not considered in this section.

In the previous study (Yoon et al., 1999), the bubble shapes in viscous liquids were analyzed using the present method and compared to the empirical correlation of Grace (1973) shown in Fig. 3. However, in this study, a constant flow condition was imposed on the top and bottom boundaries to hold the bubble in the computational domain and thus the whole process of bubble deformation from a stagnant state to a fully developed condition was not simulated. In the present calculation, a spherical bubble of radius 1 cm is placed in a stagnant liquid and rises during 0.3 s for various liquid properties. The gas–liquid interface is considered as a free-boundary as in the case of the BFC method (Ryskin and Leal, 1984). This is a good approximation when the density and viscosity of the gas are small compared with those of liquid.

Fig. 4 shows the initial distribution of computing points where the liquid channel width and height are 16 and 8 cm, respectively. Computing points are configured in four regions of (1), (2), (3), and (4) so that they fit the gas–liquid interface and are concentrated near the interface for a higher resolution. In the region (1), the computing points are distributed to fit the interface. The region (2) surrounding (1) is filled with the computing points in rectangular array. The resolution of the computing point is lowered as the distance from the interface increases. The growth ratio of the space is 1.15 for (1) and (2) while the computing points are uniformly distributed in the region (3). In the region (4), which is placed in the upper and

lower side of (3), layers of computing points are configured with a growth ratio of 1.15. The number of computing points is varied during the simulation from the initial number of 1763. The number of computing points does not need to be kept constant and the physical quantities at the re-configured points are interpolated using the convection scheme described in Section 3. No-slip condition is applied to the computing point of the wall boundary.

The bubble shapes computed by the present method are depicted in Figs. 5(a)–(f) for various liquid properties which are expressed in terms of three dimensionless numbers, i.e. Morton $M = g\mu^4/\rho\sigma^3$), Eotvos ($Eo = g\rho d^2/\sigma$), and Reynods ($Re = \rho\, Ud/\mu$) numbers. In Fig. 5(a), we can see that a spherical-cap shape is obtained at $M = 4.81 \times 10^{-13}$ and $Eo = 7.84 \times 10^{1}$ which correspond to the property of pure water. A dimpled shape is observed in Fig. 5(b) where $M = 7.84 \times 10^{1}$ with the same Eo as in Fig. 5(a). Elliptical shapes are obtained in Fig. 5(c) and (d) ($M = 9.8 \times 10^{-7}$, $Eo = 3.92$ and $M = 9.8 \times 10^{-3}$, $Eo = 3.92$), where M differs each other with the same value of Eo. When M is large, which means a strong viscous force, the aspect ratio (the ratio of the minor axis to the major axis) of the gas bubble is larger and the rising velocity is slower than the case with small M. The bubbles are spherical when the viscosity or the surface tension is large as illustrated in Fig. 5(e) and (f) ($M = 4.9 \times 10^{1}$, $Eo = 7.84$ and $M = 9.8 \times 10^{-6}$, $Eo = 3.92 \times 10^{-1}$). All the liquid states involved in the calculations (a) through (f) are indicated in Fig. 3 for the comparison with the experimental data.

The volume of the gas bubble increases as it rises in the liquid due to the decrease in the hydraulic pressure. For example, in case of (a), the gas pressure falls and the gas volume increases as the bubble rises so that $P_g \times V_g$ is constant where P_g is the gas pressure and V_g is the gas volume, respectively, as shown in Fig. 6. Although the calculations are x–y two-dimensional, the results show a good agreement with the empirical correlation of Fig. 3.

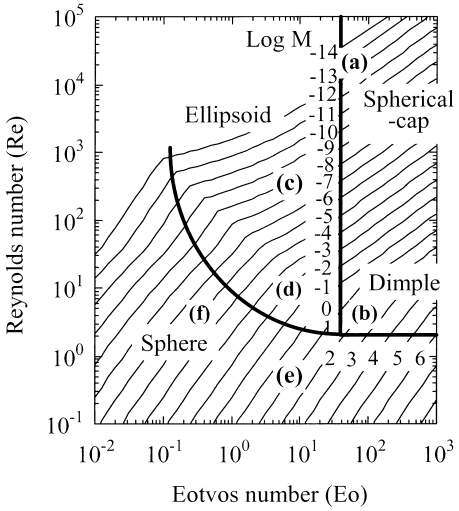

Fig. 3. Grace's graphical correlation.

5. Direct simulation of nucleate pool boiling

In this section, the energy equation of (3) is solved with the Navier–Stokes equation for the calculation of boiling. The applicability of the present method to a boiling problem was demonstrated in the previous study (Yoon et al., 1999) through the calculation of a spherical vapor bubble in uniformly superheated liquid for which a one-dimensional analytical solution was available (Plesset and Zwick, 1954). The bubble dynamics in nucleate boiling is much more complicated since the bubbles are no longer spherical and the liquid temperature is heterogeneous when they grow and depart from a heated surface. The conventional mesh-based numerical methods are not effective for this problem since it is difficult to generate fine

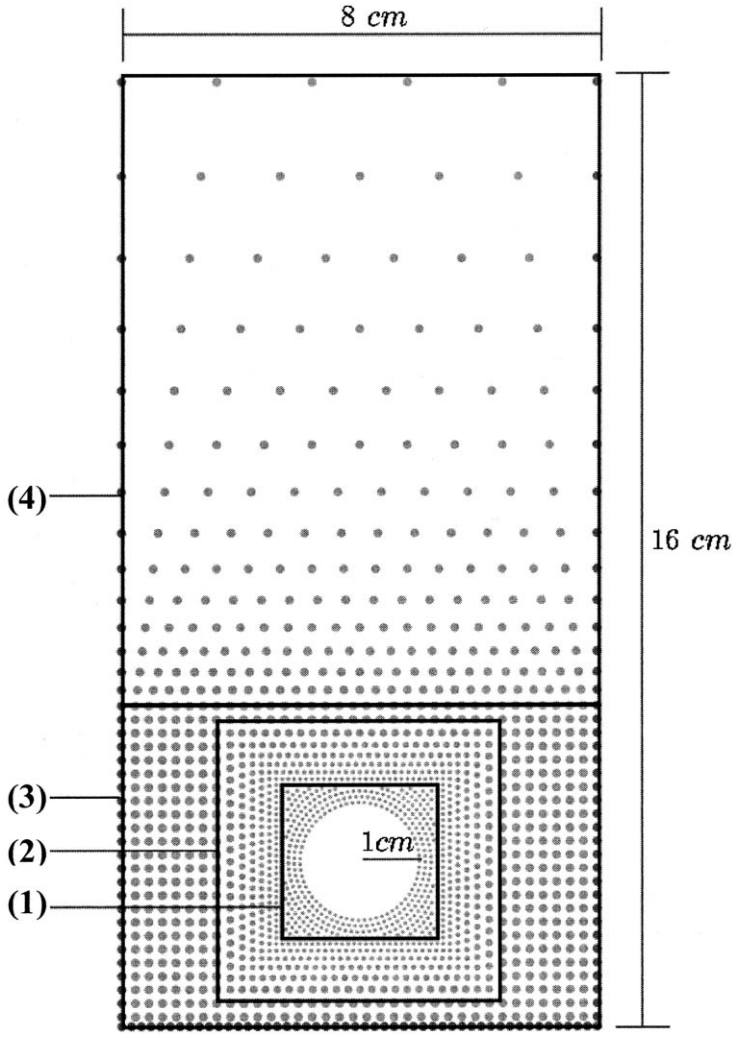

Fig. 4. Initial configuration of computing points.

meshes along the moving interface. Although there have been several numerical studies on nucleate boiling, an assumed interface shape was usually incorporated or otherwise the calculations were limited to a small deformation bubble shape. In the present study, the bubble growth and departure processes are simulated using MPS–MAFL without the assumption on the bubble shape and the numerical results are compared to the experimental data.

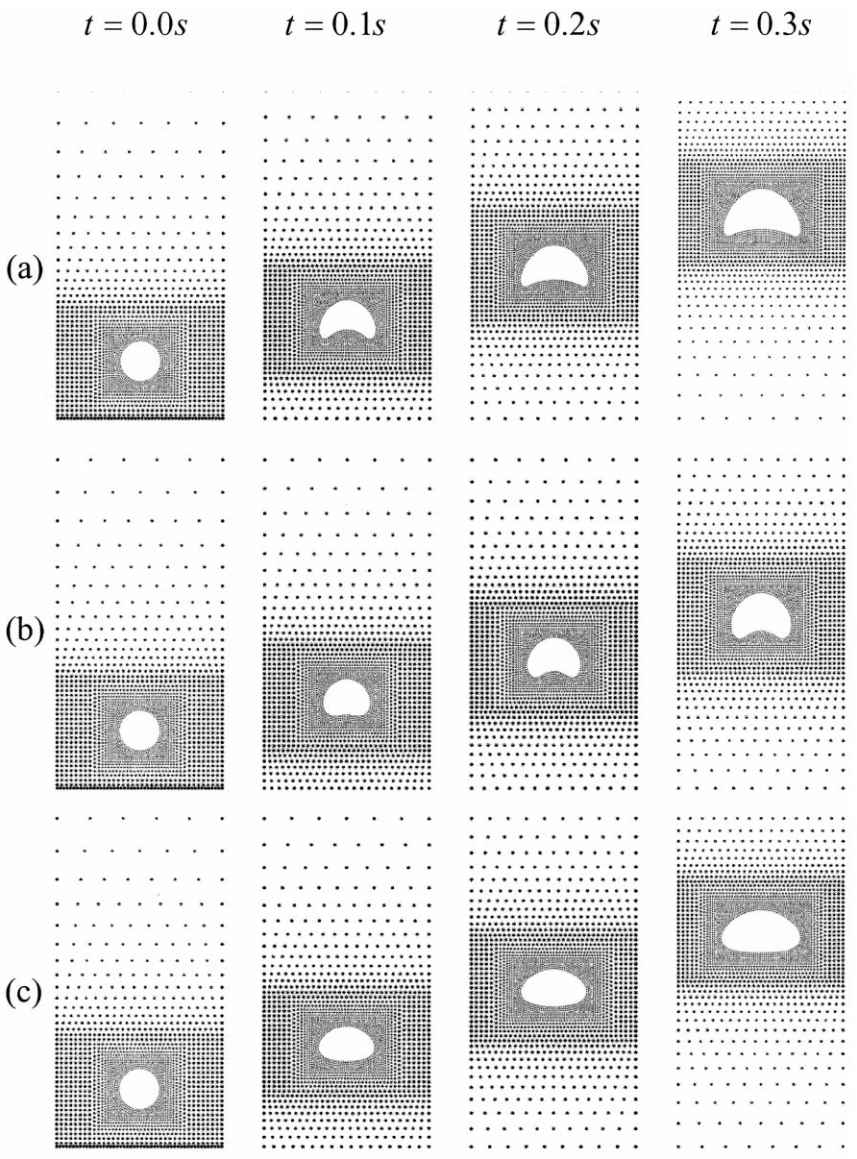

Fig. 5. Numerical simulation of rising bubble. (a) $M = 4.81 \times 10^{-13}$, $Eo = 7.84 \times 10$; (b) $M = 7.84 \times 10$, $Eo = 7.84 \times 10$; (c) $M = 9.8 \times 10^{-7}$, $Eo = 3.92$; (d) $M = 9.8 \times 10^{-3}$, $Eo = 3.92$; (e) $M = 4.9 \times 10$, $Eo = 7.84$; (f) $M = 9.8 \times 10^{-6}$, $Eo = 3.92 \times 10^{-1}$.

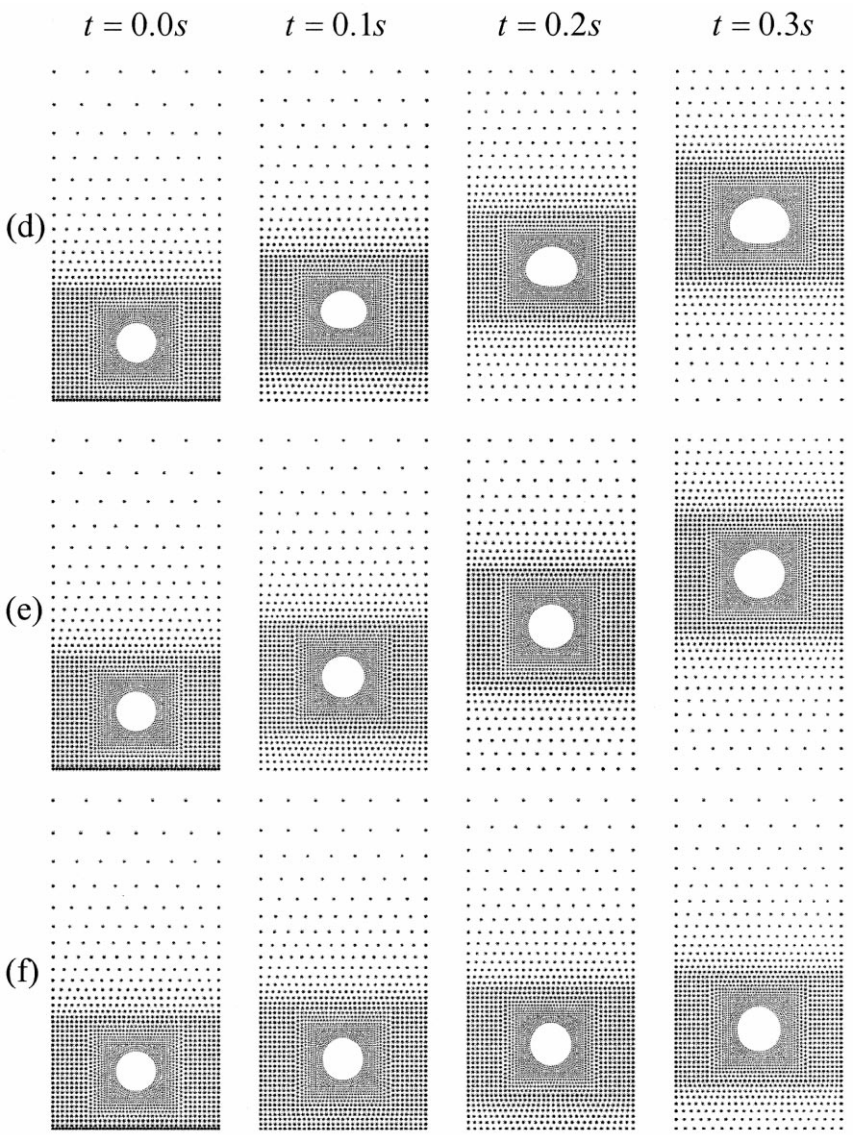

Fig. 5 (*continued*)

The calculation is based on the following physical models. First, uniform temperature and pressure are assumed for the vapor phase so that the field equations are solved only for the liquid phase. These approximations can be validated from the fact that the thermal diffusion length of the vapor is very large compared to the bubble diameter and the inertia effect of vapor is negligible in nucleate boiling at atmospheric pressure. In addition, the temperature of the phase interface is regarded as the saturation temperature for the vapor pressure (Zhang et al., 1993). The evaporation or condensation rate is obtained from the heat flux at the interface.

5.1. Bubble growth in nucleate pool boiling

Usually the bubble generation process in nucleate pool boiling is described in terms of waiting period (t_w) and growth period (t_d). During the waiting period, a transient thermal layer is formed near the heated surface before the initiation of a vapor bubble. For a given size of vapor cavity (R_c), the waiting period can be derived from the heat conduction equation for the liquid layer and the thermodynamic equilibrium condition of a vapor bubble (Han and Griffith, 1965).

$$t_w = \frac{2}{4\pi\alpha}\left\{\frac{(T_w - T_\infty)R_c}{T_w - T_{sat}\left[1 - \left(2\sigma/R_c\rho_g h_{fg}\right)\right]}\right\}^2 \tag{24}$$

where T_w is heater temperature and T_{sat} is saturation temperature.

Numerical simulations are carried out for the experiment of Han and Griffith where the data are available for the bubble growth rate, the heat flux and the number of active bubble site. The liquid (distilled water) is subcooled at 96°C with atmospheric pressure and the solid surface is heated at 110°C. The size of initial vapor bubble is 0.3 mm in radius with a contact angle 45°. The height and width of the water column are 15 and 10 mm, respectively. The waiting period corresponding to the initial bubble radius is estimated by Eq. (24) and the heat conduction calculation is performed during this waiting period to establish the initial thermal layer on the heated surface and the vapor bubble. The computing points are configured in the same way employed in Section 4 except that now the computing points are heavily concentrated near the bubble surface for the calculation of the large temperature gradient. The initial number of computing points is 4393.

Fig. 7 shows the bubble growth and departure process calculated by the present method.

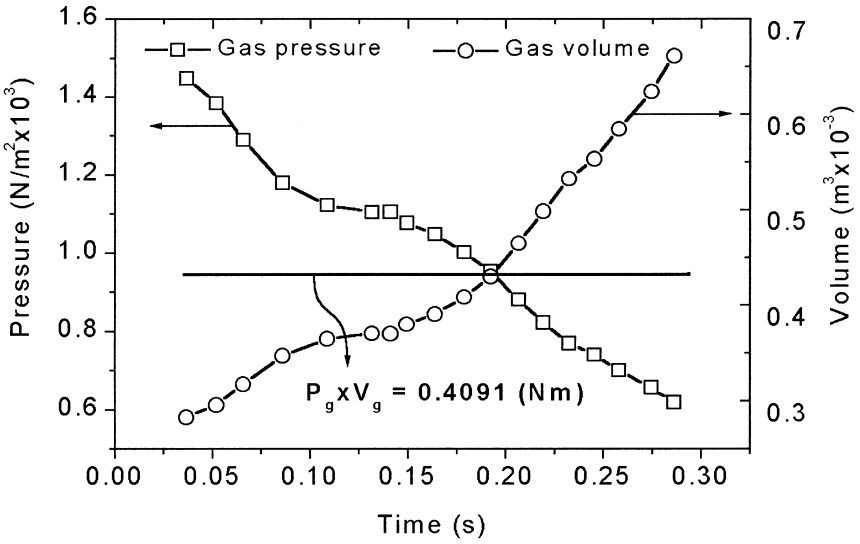

Fig. 6. Gas pressure and volume changes for Fig. 5(a).

The bubble grows fast for the first few moments due to the liquid inertia and hardly grows in the latter period where the evaporation or condensation governs the bubble growth. After the bubble departed from the heated surface, the vapor volume decreases by the condensation into the subcooled bulk liquid. In Fig. 8, the bubble growth rate calculated by the present method is compared to the experiment and the theory for homogeneous temperature fields. The bubble radii of the present calculation and the experiment grow fast in the early stage up to 5 ms and are almost constant after 10 ms while it continues to grow without the convection effect in the homogeneous theory.

5.2. Bubble departure from the heated surface

The size of vapor bubble departing from a heated surface is the function of buoyancy force attempting to detach it from the surface and the surface tension force preventing from

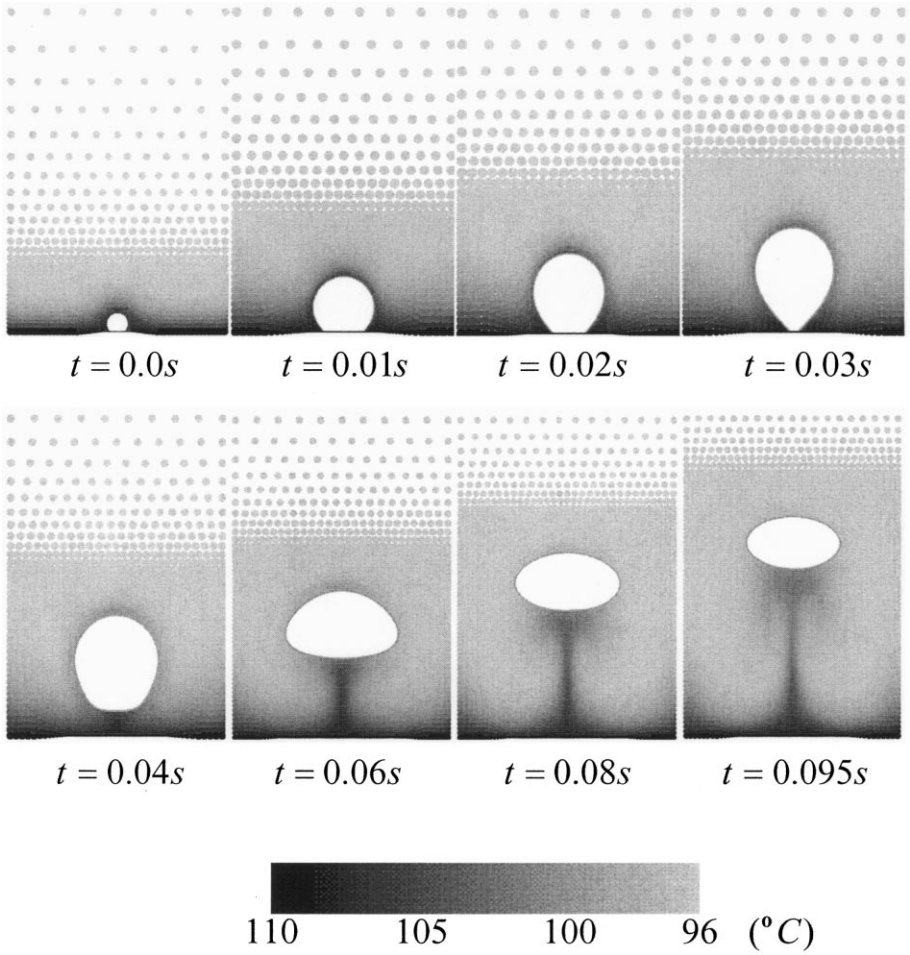

Fig. 7. Bubble growth in nucleate pool boiling (T_{wall} = 110°C, T_{sat} = 100°C, and T_{∞} = 96°C).

detachment. When the bubble grows fast, the dynamic force becomes significant so that the liquid inertia force plays an important role in determining the departure diameter. For a stagnant bubble, Fritz (1935) proposed a relation of bubble departure diameter from the balance of buoyancy force against the surface tension force.

$$D_{\mathrm{d}} \propto \theta \left[\frac{\sigma}{g(\rho_{\mathrm{f}} - \rho_{\mathrm{g}})} \right]^{1/2} \tag{25}$$

Here θ denotes the contact angle in degree. Staniszewiski (1959) proposed an empirical correlation of bubble departure diameter based on his experiments taking into account the inertia force effect:

$$D_{\mathrm{d}} \propto \theta \left[\frac{\sigma}{g(\rho_{\mathrm{f}} - \rho_{g})} \right]^{1/2} \left(1 + 0.435 \frac{\mathrm{d}D}{\mathrm{d}t} \right) \tag{26}$$

where $\mathrm{d}D/\mathrm{d}t$ is the bubble growth rate in in./s. When the bubble growth rate is small, Eq. (25) reduces to the relation of Fritz. In both cases, the bubble departure diameter is proportional to the contact angle and the square root of the surface tension constant.

The effect of surface tension and the contact angle on the departure diameter is investigated numerically using the present method. A stagnant bubble attached at the heated surface is simulated with various values of surface tension and contact angle to examine the departure diameter. The initial size of the bubble is relatively large about 1 mm so that the bubble growth rate is small. In Figs. 9 and 10, the calculated departure diameters are linearly proportional to θ and $\sigma^{1/2}$ as predicted by the Fritz's relation.

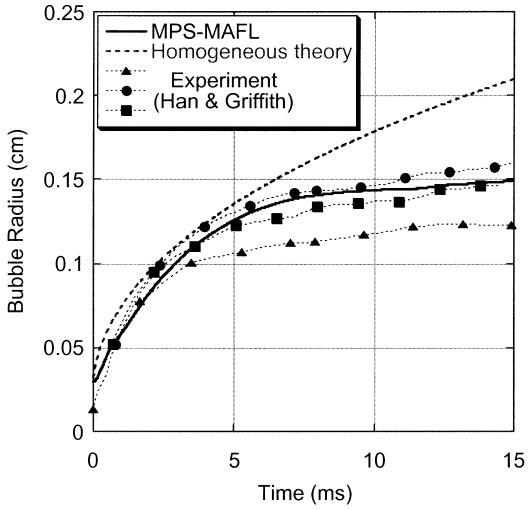

Fig. 8. Comparison of bubble growth rates.

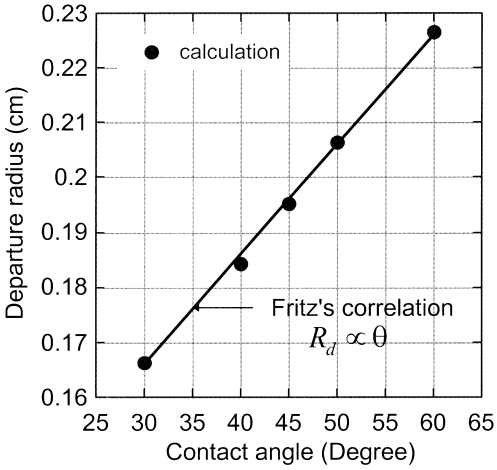

Fig. 9. Departure radius vs. contact angle.

5.3. Heat transfer mechanism

Since the numerical simulation has been performed in x–y two dimensions, an axisymmetric condition is assumed only for the calculation of the heat transferred to the liquid. For a two-dimensional computing cell i with area Δr^2 shown in Fig. 11, the volumetric energy increase is expressed as

$$\Delta q_i = \rho_f c_p \Delta T_i \Delta\ V_i \tag{27}$$

where ΔT_i is the temperature increase of a computing cell i during Δt, $\Delta V_i = 2\pi x_i \Delta r^2$, and c_p is the specific heat of fluid.

The heat transfer area is divided into two regions — the pure conduction area A_c and the

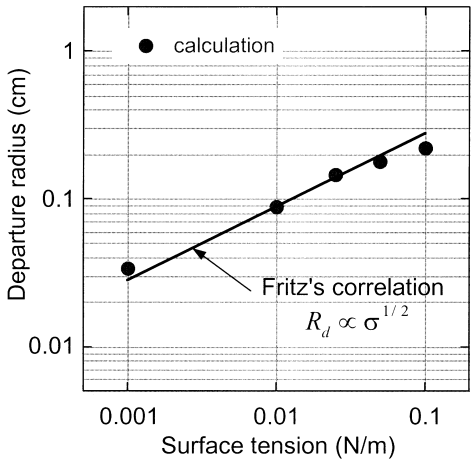

Fig. 10. Departure radius vs. surface tension.

convection area A_b influenced by the bubble motion. According to the observation of Han and Griffith, the radius of influential area is about two times of the bubble departure radius R_d so that

$$A_b = N \cdot \pi(2R_d)^2 \tag{28}$$

and

$$A_c = A_{wall} - A_b \tag{29}$$

where N is the number of active nucleate centers. Then the heat transfer rate in region A_b is calculated using Eq. (27) as follows:

$$Q_b = Nq_b = Nf\rho_f c_p \sum_{i \in A_b} \Delta T_i \Delta V_i \tag{30}$$

where f is the bubble frequency defined as $1/(t_w + t_d)$. Jacob showed that the product of a bubble frequency (f) and departure diameter (R_d) at a given nucleation cite is constant for a given operating pressure, that is

$$fR_d = \text{constant}. \tag{31}$$

Since the bubble departure diameter is almost constant by Eq. (25), the bubble frequency can be considered as constant without serious error. The conduction heat transfer rate Q_c is computed for the region A_c as the same way. The heat transfer rate due to the evaporation is obtained by

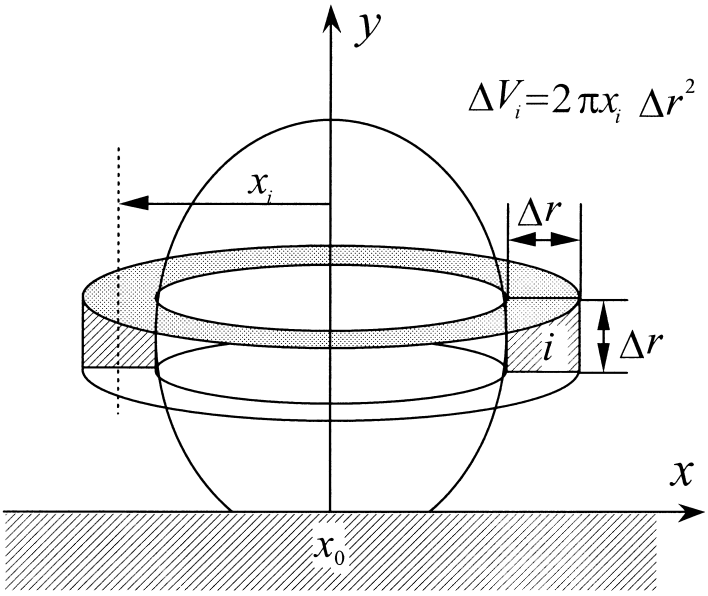

Fig. 11. Volume element of a computing point.

Table 1
Calculation of heat transfer rates

ΔT (°C) ($T_w - T_{sat}$)	N (Number of active bubbles)[a]	q_b (W)	Q_b (W) ($N \times \dot{q}_b$)	Q_c (W)	Q_{evap} (W) ($N \times \dot{q}_{evap}$)	Q_{tot} (W)
0.0	0	0.0	0.0	45.10	0.0	45.10
12.83	12	6.04	72.48	31.32	2.03	105.83
13.95	18	7.38	132.84	26.86	3.72	163.42
14.23	20	7.90	158.00	26.36	4.18	188.54
15.92	20	9.38	187.60	29.20	4.90	221.70

[a] Han and Griffith (1965).

$$Q_{evap} = Nq_{evap} \tag{32}$$

where

$$q_{evap} = \frac{4}{3} f \pi R_d^3 \rho_g h_{fg}. \tag{33}$$

In Table 1, each component of heat transfer rate computed by the present method is listed with the superheat temperature and the number of bubble nucleation site. The heat transport by evaporation occupies less than 3% and the convective heat transfer account for about 80% of the total heat transfer rate. Fig. 12 compares the computed total heat transfer rate with the experimental data and shows a pretty good agreement.

There are experimental evidences that substantiate this small contribution of latent heat to

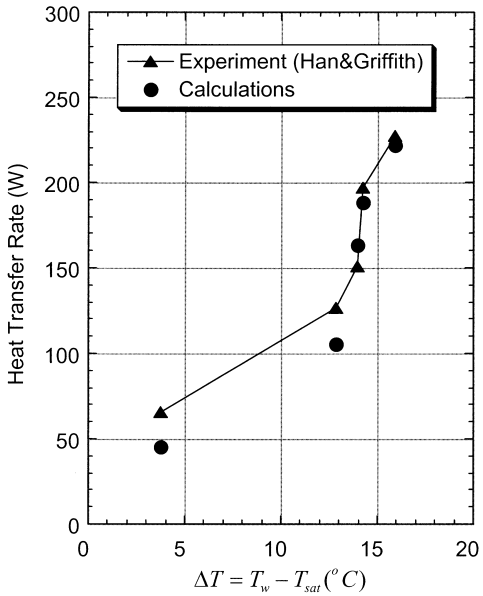

Fig. 12. Comparison of heat transfer rates.

the heat transport in surface boiling. For instance, Rohsenow et al. (1951) estimated the fraction of heat transport which can be charged to the evaporation of a vapor bubble to the total heat transport in nucleate boiling using the measured data obtained from the high-speed motion pictures of boiling process. In this study, the heat transfer fraction due to latent heat was less than 2%, and less than 10% even with the assumption of solidly packed bubbles. In the study of Forster and Grief (1959), where each component of the heat transfer mechanism in pool boiling was evaluated approximately, the latent heat transport was so small that it accounted for only 2% of the total heat flux. It was concluded, from these observations, that the high rate of heat transfer associated with nucleate boiling was primarily due to the convection of liquid layer from the motion of vapor bubbles.

Usually the heat transfer rate in nucleate pool boiling is expressed in terms of the wall superheat such that

$$Q \propto (T_{\text{wall}} - T_{\text{sat}})^n \tag{34}$$

where n is most likely 3 (Rohsenow, 1952; Levy 1959). However, the heat transfer rate which can be charged to a single vapor bubble is much less than that by Eq. (34) since the number density of vapor bubbles also increases as a function of wall superheat. By taking the number density of vapor bubbles into the consideration of the heat transfer rate, Eq. (34) can be rewritten by

$$Q \propto N^{\text{a}}(T_{\text{wall}} - T_{\text{sat}})^b \tag{35}$$

where the constants a and b are determined empirically. For instance, a is about 0.3 and b varies from 1 to 2 in the study of Zuber (1963). In Fig. 13, the calculated heat transfer rate is plotted for a single vapor bubble and it shows that the constant b is 2 in this study and within the range of empirical values.

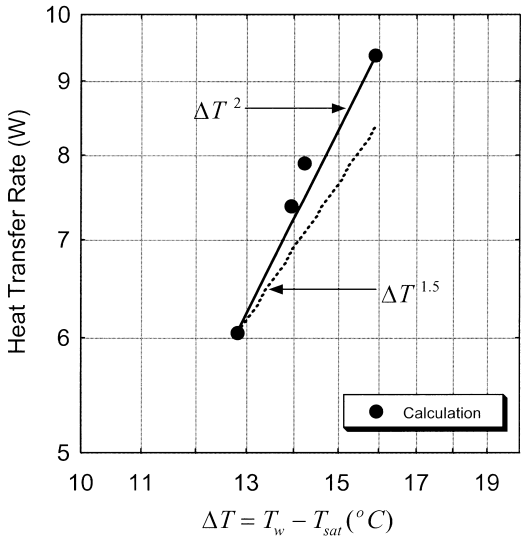

Fig. 13. Heat transfer rate per a single vapor bubble.

6. Conclusions

A mesh-free numerical method (MPS–MAFL) has been presented for the direct calculation of gas–liquid two-phase flows. The phase interface is accurately traced by the Lagrangian motion of the computing point and the large deformation of the interface is calculated effectively since the mesh structure is no longer used in the present method. The shapes of a rising bubble in stagnant viscous liquids were simulated in two dimensions and the typical bubble shapes found in the experiment were accurately reproduced for a wide range of liquid properties. The gas–liquid interface was well resolved by the local concentration of computing points.

The bubble growth and departure process in nucleate pool boiling was directly calculated using the present method. The predicted bubble growth rate well agreed with the experimental data. The computed bubble departure diameter was in proportion to the contact angle and the square root of the surface tension, which coincided with the relation of Fritz. Each component of heat transfer mechanism was evaluated quantitatively and the result showed that the high heat transfer rate in nucleate pool boiling was due primarily to the liquid agitation caused by the bubble motion.

The superheated liquid microlayer beneath the bubble is not modeled in the present calculation although there are certain evidences of its existence in nucleate boiling. It is obvious that the bubble growth rate is much influenced by the microlayer evaporation. In the present study, a superheated liquid layer is placed over the vapor bubble at the beginning of bubble formation, which may have a similar effect as the microlayer. The microlayer also enhances the heat transfer in nucleate pool boiling. Though the effect of latent heat is small in our calculation of Han–Griffith's experiment, this is not sufficient to conclude that its contribution is small in all cases of nucleate boiling since it may also depend on the conditions such as heat flux and pressure. For instance, it may be more significant for the saturated boiling in high system pressure.

In this study, the calculations were limited to the nucleate boiling with relatively low wall superheat and additional physical models for non-equilibrium vapor phase are required for the application to a wide range of two-phase boiling problems.

Acknowledgements

This study was partially supported by Grant-in-Aid for Encouragement of Young Scientists #09750178, the Ministry of Education, Science, and Culture of Japan.

References

Forster, K., Grief, R., 1959. Heat transfer to a boiling liquid — mechanism and correlations. Trans. ASME J. Heat Transfer 81, 43–53.

Fritz, W., 1935. Maximum volume of vapor bubbles. Physik Zeitschr. 36, 379–384.

Grace, J.R., 1973. Shape and velocities of bubbles rising in infinite liquids. Trans. Instn. Chem. Engrs. 51, 116–120.

Han, C.H., Griffith, P., 1965. The mechanism of heat transfer in nucleate pool boiling. Int. J. Heat Mass Transfer 8, 887–914.
Hirt, C.W., Nichols, B.D., 1981. Volume of fluid (VOF) method for the dynamics of free boundaries. J. Comput. Phys. 39, 201–225.
Hirt, C.W., Amsden, A.A., Cook, J.L., 1974. An arbitrary Lagrangian–Eulerian computing method for all flow speeds. J. Comput. Phys. 14, 227–253.
Ikeda, H., Koshizuka, S., Oka, Y., 1996. Numerical analysis of multi-phase multi-fluid flow with vaporization using MPS. In: Proc. 8th Comput. Mech. Conf., Fukuoka, Nov. 27–29 (in Japanese).
Koshizuka, S., Oka, Y., 1996. Moving-particle semi-implicit method for fragmentation of incompressible fluid. Nucl. Sci. Eng. 123, 421–434.
Koshizuka, S., Oka, Y., 1998. Numerical analysis of breaking waves using the moving particle semi-implicit method. Int. J. Numer. Meth. Fluids 26, 751–769.
Koshizuka, S., Yoon, H.Y., Yamashita, D., Oka, Y., 2000. Numerical analysis of natural convection in a square cavity using MPS–MAFL. Compt. Fluid Dynamics J. 8, 485–494.
Lee, R.C., Nydahl, J.E., 1989. Numerical calculation of bubble growth in nucleate boiling from inception through departure. J. Heat Transfer 111, 474–479.
Levy, S., 1959. Generalized correlation of boiling heat transfer. Trans. ASME J. Heat Transfer 81, 37–42.
Plesset, M.S., Zwick, S.A., 1954. The growth of vapor bubbles in superheated liquids. J. Applied Phys. 25, 493–500.
Rayleigh, L., 1917. On the pressure devepoled in a liquid during the collapse of a spherical cavity. Phil. Mag. 34, 94–98.
Rhie, C.M., Chow, W.L., 1983. Numerical study of turbulent flow past an airfoil with trailing edge separation. AIAA Journal 21, 1525–1532.
Rohsenow, W.M., Clark, J.A., 1951. A study of the mechanism of boiling heat transfer. Trans. ASME 73, 609–620.
Rohsenow, W.M., 1952. A method of correlating heat-transfer data for surface boiling of liquids. Trans. ASME 74, 969–976.
Welch, S.W.J., 1995. Direct simulation of vapor bubble growth. Int. J. Heat Mass Transfer, 41, 1655–1666.
Ryskin, G., Leal, L.G., 1983. Orthogonal mapping. J. Comput. Phys. 50, 71–100.
Ryskin, G., Leal, L.G., 1984. Numerical solution of free-boundary problems in fluid mechanics. J. Fluid Mech. 148, 1–43.
Staniszewiski, B.E., 1959. Nucleate boiling bubble growth and departure. MIT Tech. Rept. No. 16, Div. of Sponsored Research, Cambridge, MA.
Welch, J.E., Harlow, F.H., Sharmon, J.P., Daly, B.J., 1966. The MAC method. LA-3425.
Yoon, H.Y., Koshizuka, S., Oka, Y., 1999. A particle-gridless hybrid method for incompressible flows. Int. J. Numer. Methods in Fluid 30, 407–424.
Yoon, H.Y., Koshizuka, S., Oka, Y., 1999. A mesh-free numerical method for direct simulation of gas–liquid phase interface. Nucl. Eng. Sci. 133, 192–200.
Zhang, Q., Hewitt, G.F., Leslie, D.C., 1993. Nuclear safety code modelling of condensation in stratified flow. Nucl. Eng. Design 139, 1–15.
Zuber, N., 1963. Nucleate boiling. The region of isolated bubbles and the similarity with natural convection. Int. J. Heat Mass Transfer 6, 53–78.